Dual Carbon Design Strategy for Anodes of Sodium Ion Battery: Mesoporous CoS_2/CoO on Open Framework Carbon-spheres with rGO Encapsulating

Ran Sui[a,†], Guangtao Zan[a,†], Ming Wen[a,], Weina Li[a], Zihui Liu[a], Qingsheng Wu[a], YongQing Fu[b]*

a School of Chemical Science and Engineering

Shanghai Key Laboratory of Chemical Assessment and Sustainability

Tongji University

Shanghai 200092, P. R. China.

b Faculty of Engineering and Environment

Northumbria University

Newcastle Upon Tyne NE99, UK

KEYWORDS. CoS_2, CoO, Open framework carbon-sphere, Graphene, Heterojunctions, Dual carbon strategy, Anode, Sodium-ion battery

ABSTRACT Transition metal sulfides and oxides with high theoretical capacities have been regarded as promising anode candidates for sodium-ion battery (SIB); however, they have critical issues including sluggish electrochemical kinetics and poor long-term stability. Herein, a dual carbon design strategy is proposed to integrate with highly-

active heterojunctions to overcome the above issues. In this new design, CoS_2/CoO hollow dodecahedron heterojunctions are sandwiched between open framework carbon-spheres (OFCs) and reduced graphene oxide (rGO) nanomembrane (OFC@CoS_2/CoO@rGO). The CoS_2/CoO heterojunctions effectively promote electron transfer on their surface and provide more electrochemical active sites through their hierarchical hollow strucutres assembled by nanodots. Meanwhile, the dual-carbon framework forms a highly conductive network that enables a better rate capability. More importantly, the dual carbon can greatly buffer volume expansion and stable reaction interfaces of electrode material during charge/discharge process. Benefitting from their synergistical effects, the OFC@CoS_2/CoO@rGO electrode achieves a high reversible capacity of 460 mAh g^{-1} at 0.05 A g^{-1} and still maintains 205.3 mAh g^{-1} even when current density is incresed by 200 times when used as an anode material for SIBs. Their cycling property is also remarkable with a maintained capacity of 161 mAh g^{-1} after 3500 charging/discharging cycles at a high current density of 1 A g^{-1}. The dual-carbon strategy is demonstrated to be effective for enhanced reaction kinetics and long-term cycling property, providing siginificant guidance for preparing other high-performance electrode materials.

1. Introduction

Sodium-ion battery (SIB), as a new energy storage system, has merits of low cost and abundant reserves, and thus been regarded as an ideal candidate to replace the commonly used lithium-ion battery (LIB) for large-scale energy-storage systems.[1-3]

However, the SIBs have many issues to be solved before their commercial applications.[4] Among these, the electrode material becomes the dominant factor to limit its electrochemical performance in practical applications. Although the chemical properties of sodium (Na) are very similar to those of lithium (Li), Na^+ ions (1.02 Å) have a larger radius than Li^+ ions (0.76 Å), which reduces the ionic migration efficiency and intensifies pulverization during cycling of the SIB.[5-7] Therefore, there is a critical demand to search for the anode material for the SIB with a high reversible capacity, fast reaction kinetics, and good structural stability. The anode materials for the SIB can be classified into three major categories according to their reaction mechanisms, i.e., the insertion type, the conversion type, and the alloying type.[8] They all have various problems, e.g., the low theoretical capacity for the insertion type, severe volume expansion, and poor cyclic stability for the alloying type and conversion type.[9-12] A common solution for these issues is to combine high-capacity but poor-cyclability materials with the conductive and stable skeletons to comprehensively improve the overall electrochemical performance.[13, 14]

Transition metal chalcogenides (TMCs), especially Co-based materials, have high theoretical capacities, mainly attributed to their multielectron reaction abilities with Na^+ ions.[15-19] For example, mesoporous $Cu_{2-x}Se$ nanocrystals present a capacity retention of 88 % after 3000 cycles at 5 A g^{-1} (212.4 mAh g^{-1}).[20] CoS_2 showed a reversible discharge capacity of 724 mAh g^{-1} and could be stabilized by combining with multiple wall carbon nanotubes (MWCNTs).[21] Nanostructured Co_3O_4 delivered a reversible capacity of 447 mAh g^{-1} over 50 cycles at 0.05 A g^{-1}.[22] $FeS_{2-x}Se_x$ combines the

advantages of FeS_2 and $FeSe_2$ and achieves high stability and high-rate performance.[23] However, there are few studies on using CoS_2/CoO heterojunctions for electrodes of the SIB. Porous heterojunction nanoparticles are effective to increase the electrical conductivity of metal sulfides, provide more active sites for the conversion of Na^+ as well as the decomposition of irreversible SEI layers, and increase the atomic utilization, thus improving the sodium storage capacity of the electrode materials. On the other hand, many carbon materials have been explored as the skeletons of SIBs' anode materials, such as hard carbon, graphene, and carbon nanofibers.[24] For example, a VS_4/rGO composite with a rGO skeleton produced a discharge capacity of ~241 mAh g^{-1} at 0.1 A g^{-1} after 50 cycles.[25] CoPSe@layered N-doped carbon prepared by layered zeolitic imidazolate frameworks (ZIFs) achieved a capacity of 303 mAh g^{-1} at 0.2 A g^{-1} over 500 cycles.[26] As one type of metal-organic frameworks (MOFs), ZIFs can be used as the precursors to synthesize a variety of porous materials. Although these carbon skeletons play positive roles in enhancing the dispersion, conductivity, and capacity of the composites, simply using the skeleton is still limited in enhancing the cycling stability of the anode materials. [11, 27, 28] The combination of carbon skeletons within different dimensions can not only elastically prevent the inflation and ensure the structural integrity but also immensely improve the conductivity and endow high-rate properties, which is an effective and general approach to improve the performance of conversion and alloying materials.[29, 30] Therefore, we believe that, if highly active heterojunctions are integrated with appropriately designed dual-carbon skeletons, a

high-performance anode material and a novel composite structure for SIBs will be obtained.

In this work, ZIF-67 was chosen as precursors to construct the highly active CoS_2/CoO heterojunctions through the sulfidation of ZIF and partial reduction of carbon. Dual-carbon skeletons are designed to integrate internal open framework carbon-spheres (OFC) and external rGO nanomembrane encapsulating (see **Figure 1**). By combing them together, a sandwich structure of OFC@CoS_2/CoO@rGO is obtained (Figure 1). When applied as the anode material for the SIB, benefitted from the special features and their synergistic effects, both the rate capability and cycling performance remarkably improved. The specific capacity can maintain ~50% when current density is increased by 200-fold from 0.05 to 10 A/g. Reversible capacities of 423 and 353 mAh g^{-1} have been achieved after 100 and 250 cycles at a current density of 100 mA g^{-1}. Notably, even after cycling for 3,500 times at a high current density of 1 A g^{-1}, it still maintains a reversible capacity of 161 mAh g^{-1} with a Coulomb efficiency of 99.6 %. The integration of dual-carbon design with heterojunction not only achieves a high-performance anode material for SIB, but also provides important references for the preparation of other similar electrode mateirals.

2. Experimental Section/Methods

2.1. Chemicals

Most of the chemicals were purchased from Aladdin Reagents, Shanghai, China, including sodium chloroacetate ($ClCH_2COONa$, 99%), methanol (CH_4O, ≥99.5%), cobalt nitrate ($Co(NO_3)_2 \cdot 6H_2O$, ≥99%), carbon disulfide (CS_2, AR), 2-methylimidazole

($C_4H_6N_2$, ≥98%), polyvinyl-pyrrolidone ($(C_6H_9NO)_n$, PVP, M.W.1300000), ethylene imine polymer $(CH_2CH_2NH)_n$, M.W.600, 99%), 1-(3-Dimethylaminopropyl)-3-ethylcarbodiimide hydrochloride ($C_8H_{18}ClN_3$, 98.0%) and graphene oxide gel (GO, 1-3wt%). Powder of sulfur (S_8, ≥99.0%) was purchased from Sigma -Aldrich. Sodium-ion battery electrolyte (1.0M NaClO4 in EC:PC=1:1 Vol% with 5.0%FEC) was purchased from Suzhou Duoduo Chemical Technology Co., LTD. Conductive carbon black (ECP600JD) was commercially available from Lion Corporation, Japan. All the chemicals were used without further purification.

Preparation of OFC@CoS_2/CoO@rGO

Preparation of Open-framework Carbon Spheres (OFCs). Firstly, the OFC was prepared by a one-step aerosol approach using an ultrasonic spray pyrolysis (USP) method. In brief, a humidifier operated at a frequency of 1.7 MHz was used to nebulize the precursor solution (sodium chloroacetate, $ClCH_2COONa$, 1.5 mol/L) into fine droplets. The generated droplets were then carried away by the argon flow (1~3 L/min) into a furnace (500~900 °C). The black powders after the pyrolysis were collected in ethanol bubblers. After reaction, the final products were washed and centrifuged with ethanol (50 vol.%) for three times and dried in a vacuum oven at 60 °C.

*Preparation of aminated GO aqueous solution***.** The aminated GO solution was converted from the commercially purchased GO gel. The GO gel (1-3 wt%, Aladdin) was prepared into a solution of 0.5 mg/mL, and then 10 mg/mL polyethylene imine was added under a continuously ultrasonic agitation, and the pH value was adjusted to 8. After half an hour, 3 mg/mL 1-(3-Dimethylaminopropyl)-3-ethylcarbodiimide

hydrochloride was added. The obtained liquid was stirred continuously for 24 h to obtain an aqueous solution of aminated GO.

Preparation of OFC@CoS_2/CoO@rGO. In a typical procedure, the prepared OFC of 10 mg was dispersed inside the methanol solution, followed by the successive addition of 100 mg of PVP, 0.5 mmol of cobalt nitrate and 4 mmol of 2-methylimidazole. The mixed solution was stirred continuously at room temperature for 4 h to obtain a purple precursor of OFC@ZIF-67. During the following transformation synthesis process, the obtained OFC@ZIF-67 precursors and sulfur powders were placed in the rear and front of a tube furnace, respectively. The furnace was heated to 400 ℃ and held for 2 h in a N_2 atmosphere. After that, the obtained black powder was washed with reflux carbon disulfide (CS_2) for 2 h to obtain OFC@CoS_2/CoO. A certain OFC@CoS_2/CoO was dispersed in water to form a concentration of 1 mg/ mL. The same amount of preaminated GO with positive surface was added slowly under stirring, which made the GO well-capsulized onto the surface of OFC@CoS_2/CoO. Finally, OFC@CoS_2/CoO@rGO was obtained after a calcination process at 400 ℃ for 2h in N_2 in a furnace.

Preparation of CoS_2@rGO. CoS_2@rGO was prepared as the control group sample by the same procedure as OFC@CoS_2/CoO@rGO, except that the OFC was not added in the preparation process.

2.2. Characterization

Morphologies and microstructures of the samples were characterized using a field emission scanning electron microscope (FE-SEM, Hitachi, S-4800) and a transmission electron microscope (TEM, JEOL, JEM-2100EX). An EDS (Oxford, TN-5400)

attached to the SEM was used to obtain the contents and distributions of the samples' elements. Crystalline structures of the samples were analyzed on a powder X-ray diffractometer with Cu Kα radiation (λ= 0.154056 nm) (XRD, Bruker, D8 Advance). An X-ray photoelectron spectrometer (XPS, Kratos, AXIS Ultra DLD, Al Kα source) was used to determine chemical bonding information on elements. The obtained values of electron binding energy were calibrated according to the value of adventurous carbon (C 1s, 284.6 eV), and the data analysis was carried out using XPS Peak 41 software. A Raman spectrometer (Raman, inVia, Renishaw) and Fourier transform infrared spectrometer (FT-IR, Thermo Scientific, Nicolet iS10) were applied to identify the molecular structures and bonding modes of the samples. The surface area of the sample was obtained using a porosity analyzer (Micromeritics, Tristar 3020), and the adsorption isotherm was measured at -196 ℃. The specific surface areas and pore diameter distributions of the samples were obtained by Brunauer-Emmett-Teller (BET) and BJH models, respectively. Thermogravimetric (TG) analysis was carried out on a STA 409 thermal analyzer with a heating rate of 5 °C min^{-1} in a flowing air atmosphere. A ζ potential analyzer (Litesizer 500) was used to obtain the surface potentials of samples.

2.3. Electrochemical measurements

Electrochemical measurements were performed using the CR2016 coin-type cells assembled in an argon-filled glove box. To prepare the working electrodes, active substance, conductive carbon black and polyvinylidene fluoride binder with a mass ratio of 8:1:1 were mixed uniformly in the N-methyl pyrrolidone to form a slurry. The obtained slurry was then uniformly coated onto a copper foil with a thickness of 150

μm and dried overnight in a vacuum oven at 70 ℃. Subsequently, the coated copper foil was punched into wafers, and the mass loading on the wafer was 1.5±0.1 mg/cm^2. Sodium metal and glass fiber were used as the counter electrode and separator, respectively. Galvanostatic electrochemical experiments were conducted using a multichannel battery test system (LAND CT2001A) at 25 ℃. The cyclic voltammetry curves (CV) and electrochemical impedance spectroscopy (EIS) were carried out using a Princeton Applied Research VersaSTAT4 electrochemical workstation. The specific capacities of all the samples were calculated based on the total mass of active materials.

3. Results and discussion

3.1. Morphology and Structure

Figure 1 shows schematic views of fabrication and sodiation/desodiation processes of the hierarchically porous composites (OFC@CoS_2/CoO@rGO). First, the ZIF-67 dodecahedrons were decorated onto the OFC, which is prepared by ultrasonic spray pyrolysis (**Figure S1 and S2, Supporting Information**). Then the prepared OFC@ZIF-67 was *in situ* transformed onto OFC@CoS_2/CoO via the sulfurization and partial reduction process of carbon. Afterwards, preaminated GO with its positive potential on the surface was employed to capsulize the OFC@CoS_2/CoO through an electrostatic self-assembly process **(Figure S3)**. Finally, the sample was annealed under N_2 to form OFC@CoS_2/CoO@rGO, which contains dual carbon skeletons and highly active CoS_2/CoO heterojunctions. The optimized sandwich structure is based on the stable rigid carbon skeleton with a hierarchically porous morphology (**Figure S4-S6**). Such a porous morphology can reduce the volume expansion effect, and facilitate mass transfer, thus enhancing the Na^+ storage as the anode material.

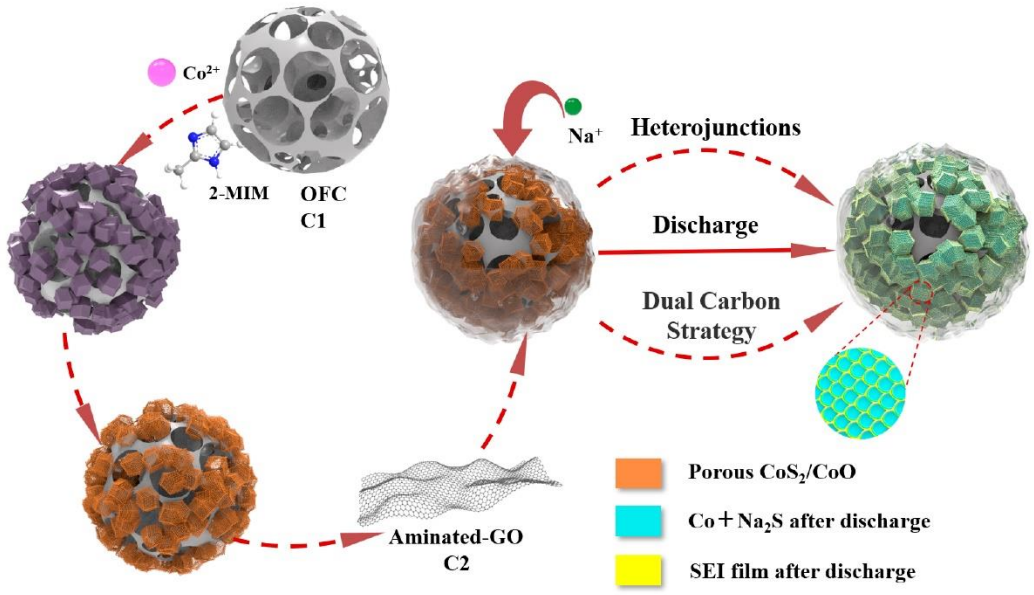

Figure 1. Illustrations of 3D structures and synthesis procedures of sandwich and porous nanostructured spheres of OFC@CoS_2/CoO@rGO and its sodiation/desodiation process.

Figure 2 shows morphologies and microstructures of the prepared samples. The internal 3D carbon skeleton is an open framework, having abundant cross-linked macropores (**Figure 2a**), which can provide abundant spaces for mass transfer and surface decoration. The smooth ZIF-67 dodecahedrons can be uniformly located on these OFCs with an average inner channel size of ~200 nm (**Figure 2b**). After their *in-situ* transformation, the CoS_2/CoO heterojunctions with mesoporous structures were formed, and they display similar morphologies to those of ZIF-67 except that their surfaces are much coarser (**Figure 2c and 2d**). TEM image indicates that CoS_2/CoO structures are hollow and distorted dodecahedrons assembled by evenly distributed nanoparticles with an average size of ~20 nm (**Figure 2e**). Such small building blocks can expose more surface atoms and provide higher activities for electrochemical

reactions.[31] When they are further encapsulated with highly flexible and strong graphene membranes, the targeted product of OFC@CoS_2/CoO@rGO is obtained, and **Figures 2f,g** show their SEM and TEM images. Its selected area electron diffraction (SAED) pattern exhibits diffraction rings, indicating their polycrystalline structure. These diffraction rings can be indexed to (200) and (210) planes of the CoS_2 crystal. A high-resolution transmission electron microscopy (HRTEM) image exhibits lattice fringes with interplanar spacings of 2.45 Å, 2.48 Å and 2.81 Å (**Figure 2h**), which can be assigned to the (111) plane of CoO crystal and (200) and (210) planes of the CoS_2 crystal, respectively. The TEM analysis results are consistent with those of the SAED, demonstrating the formation of CoS_2/CoO. The elemental dot mapping with EDS analysis shown in **Figure 2i** demonstrates the existence of C, Co and S elements, and they are evenly distributed inside the OFC@CoS_2/CoO@rGO.

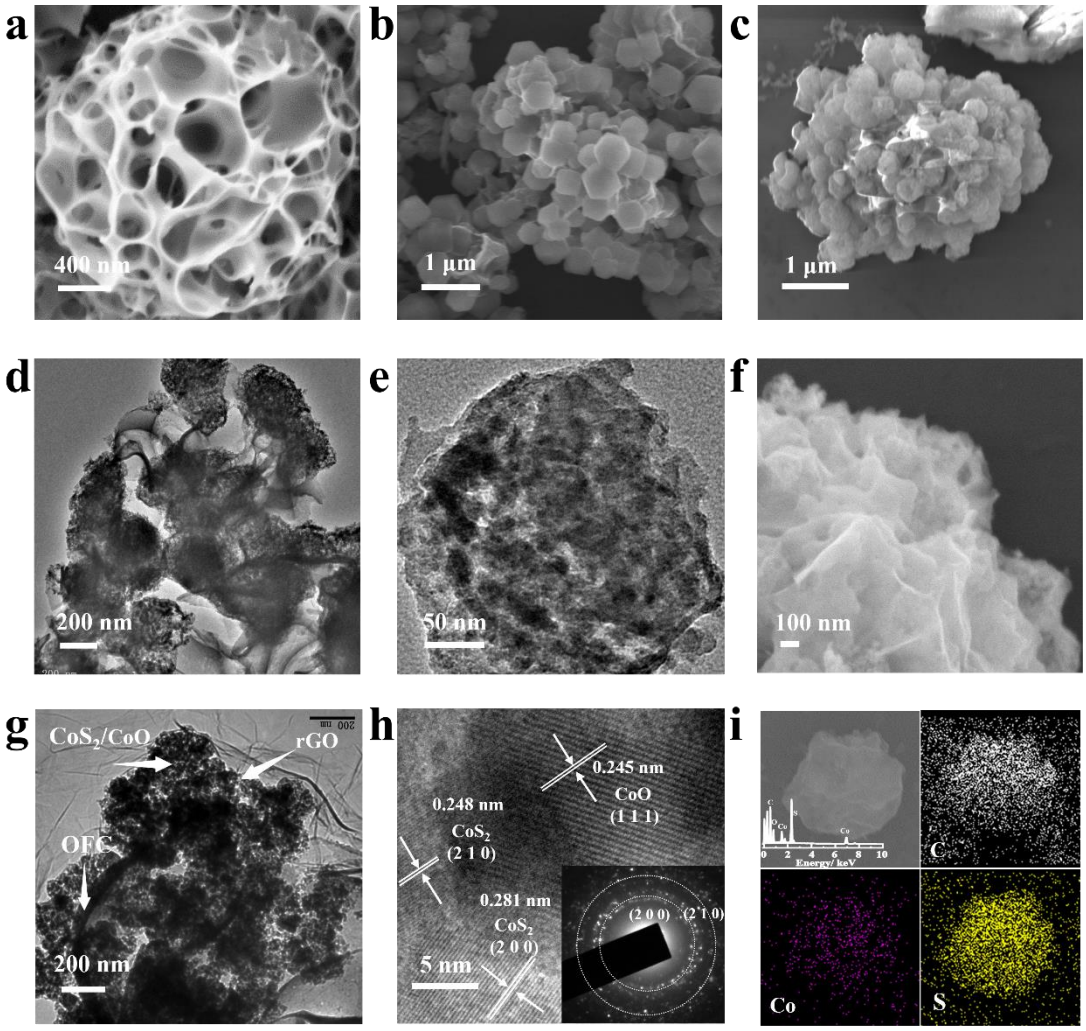

Figure 2. Morphology characterization. (a-c) SEM images of OFC, OFC@ZIF-67, and OFC@CoS_2/CoO, respectively; (d and e) TEM images in different magnifications of OFC@CoS_2/CoO, (f) SEM image, (g) TEM image, (h) HRTEM image with inset SAED pattern, and (i) elemental mapping with EDS of OFC@CoS_2/CoO@rGO.

Figure 3a shows XRD pattern of OFC@CoS_2/CoO, which display four major peaks at the positions 32.3°, 36.2°, 46.3° and 54.9°, corresponding to the (200), (210), (220) and (311) crystal planes of CoS_2, respectively. [32, 33] Two weak diffraction peaks can also be observed at 36.5° and 42.4° in the XRD pattern, which conforms to the (111) and (200) crystal planes of CoO, indicating the existence of CoS_2/CoO heterojunction. [34]

The diffraction peaks of OFC@ZIF-67 precursor disappear (**Figure S2b**). This result is consisted with the XRD pattern of CoS_2 converted from ZIF-67 (**Figures S7 and S8**). After OFC@CoS_2/CoO is capsulated with rGO, the XRD pattern shows a broad peak at ~21.2°, which is corresponding to the diffraction peak of the (002) plane of graphite.[35] It is well-known that, in the Raman spectra of a carbon material, the D peak (1341 cm^{-1}, stand for disorder) is the characteristic disordered carbon with structural defects, whereas the G peak (1587 cm^{-1}, stand for graphite carbon) is associated with graphite carbon.[36, 37] Their peak strength I_D and I_G are proportional to the contents of disordered and ordered carbon atoms, respectively. The obtained ratio values of I_D/I_G for samples of OFC, OFC@CoS_2/CoO and OFC@CoS_2/CoO@rGO are 0.67, 0.98, and 0.92, respectively (**Figure 3b**). This reveals that most of the carbon atoms exist in sp^2 type, which could enhance the electrical conductivity.[38] The synthesis process of OFC@CoS_2/CoO@rGO can be confirmed by the FT-IR analysis. FT-IR spectrum of GO reveals the peaks with wave numbers of ~3250 cm^{-1} and ~1650 cm^{-1}, revealing the presence of -NH_2 and -COOH on the surface of GO (**Figure S9**).[39, 40] High-temperature treatment under the N_2 results in significantly decreased intensities for these peaks, indicating that the GO has been reduced into rGO. To further understand the valence and bond information of OFC@CoS_2/CoO@rGO, XPS analysis was performed. The survey spectrum **(Figure 3c)** demonstrates the existence of C, Co, S elements. The spectrum of C 1s can be divided into three peaks. The single peak at 284.6 eV is exclusively attributed to C=C bonds without any traces of other bonds, and higher BEs of 286.3 and 289.0 eV are corresponding to those of C–O/C-S and C=O, respectively

(**Figure 3d**).[41, 42] The Co 2p spectrum (**Figure 3e**) can be deconvoluted into three pairs of peaks, i.e., Co-S bonds (782.1 eV and 798.8 eV), Co-O bonds mainly due to the partial reduction of OFC (778.8 eV and 793.5 eV), and satellite peaks of $Co_{2p1/2}$ and $Co_{2p3/2}$, respectively.[43] The S 2p spectrum can be deconvoluted into two pairs at 169.0 and 170.1 eV, 165.1 and 163.9 eV, which are assigned to S^{2-} and S-O bonds, respectively (**Figure 3f**).[44] All the XPS analysis results confirm the formation of CoS_2/CoO on OFC. N_2 adsorption test reveals that the OFC@CoS_2/CoO@rGO has a specific surface area of 74.06 m^2 g^{-1} with an average pore diameter of ~5.9 nm (**Figure S10**). TG analysis under air shows the mass contents of CoS_2, CoO and carbon in the composite are 30.45%, 4.55% and 65%, respectively (**Figure S11**). Such highly porous structures can facilitate effective diffusions of Na^+ ions and infiltration of electrolyte, which can enhance the electrochemical performance.

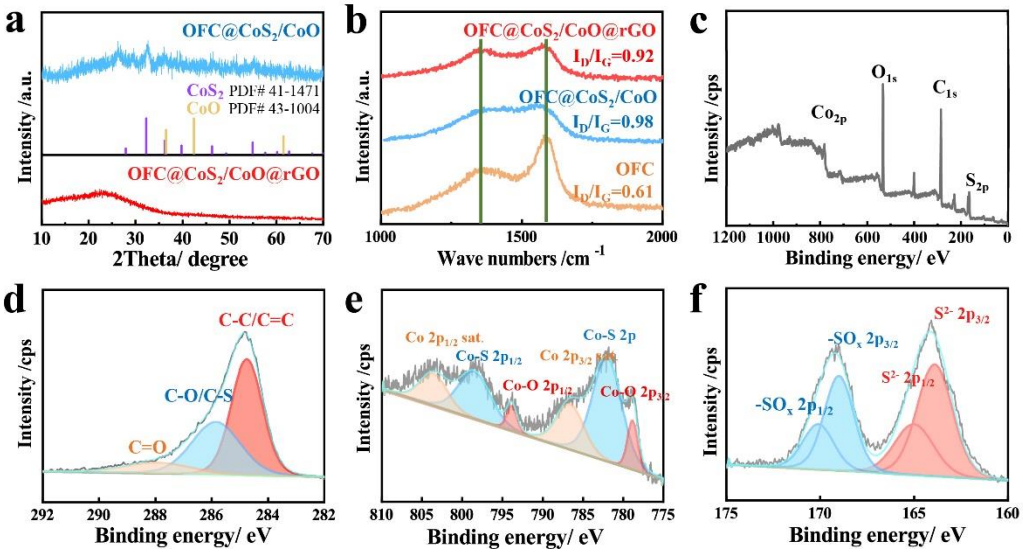

Figure 3. Structural characterization. (a) XRD patterns and (b) Raman spectra of the prepared samples; (c-f) full XPS and high-resolution XPS spectra of OFC@CoS_2/CoO@rGO.

3.2. Electrochemical performance

Figure 4 presents the electrochemical performance of OFC@CoS_2/CoO@rGO as an anode material for SIBs. In all the tests, half coin cells with sodium metal as the counter electrode were used. The cyclic voltammetry (CV) curves of the initial three cycles show its operation potential window from 0 to 3 V vs. Na/Na^+ (**Figure 4a**). The first CV curve exhibits two irreversible reduction peaks at 1.0 and 0.6 V during its discharge process, but they disappear in the following two cycles, clearly indicating the formation of a layer of SEI film afterward.[45, 46] In the following two cycles, only the reduction peaks concentrated at ~0.8 V appear during the discharge process, which are associated to the reactions (1) and (2). While all the three CV cycles show the same oxidation peaks at ~1.6 V, which is associated with the reaction (3).[21]

$$CoS_2 + xNa^+ + xe^- \rightarrow Na_xCoS_2 \quad (1)$$

$$Na_xCoS_2 + (4-x)Na^+ + (4-x)\,e^- \rightarrow Co + 2Na_2S \quad (2)$$

$$Co + 2Na_2S \rightarrow CoS_2 + 4Na^+ + 4e^- \quad (3)$$

Its CV curves after the first test overlap well, revealing the fast stability feature which is benefitted from its composite structure. Similar peak positions can also be observed in the results of OFC@CoS_2/CoO and CoS_2@rGO (**Figures S12a and S13a**), demonstrating their similar electrochemical behaviors to the anode for SIBs. The galvanostatic charge/discharge (GCD) profiles of OFC@CoS_2/CoO@rGO half cell tested at 0.05 A g^{-1} are displayed in **Figure 4b**. The GCD curves present one discharge plateau at 0.9 V and one charge plateau at 1.6 V, consistent with the positions of main reduction and oxidation peaks in the CV curves, respectively, whereas the 2nd and 3rd

charge/discharge curves of OFC@CoS_2/CoO@rGO are more consistent, which is dramatically different from those of OFC@CoS_2/CoO and CoS_2@rGO (**Figures S12b and S13b**). These results demonstrate that the OFC@CoS_2/CoO@rGO has the optimal structure to realize interfacial stability among these three samples, whereas the OFC@CoS_2/CoO without encapsulated by the rGO shows the worst stability performance. The results clearly manifest that the significantly improved cycling property is attributed to the layer of encapsulated rGO via stabilizing reaction interfaces and restricting the volume expansion. These result in a good rate performance and a stable reversible capacity of 205.3 mAh g^{-1}, even after the current density is increased up to 10 A g^{-1}. This value is much higher than those of OFC@CoS_2/CoO and CoS_2@rGO (**Figure 4c**). When the current density is decreased to 0.05 A g^{-1}, the capacity of the OFC@CoS_2/CoO@rGO almost recovers to its initial value. The OFC@CoS_2/CoO@rGO electrode exhibites a characteristic voltage plateau when charging/discharging processes are performed under these currents (**Figure 4d**), suggesting that the structure of the electrode material has not been apparently damaged by the volume expansion effect during the rapid charge and discharge processes. Analysis of electrochemical impedance spectroscopy (EIS) of the OFC@CoS_2/CoO@rGO was further performed after activation. In a typical Nyquist diagram, the radius of the high-frequency semicircle reflects the scale of the charge transfer resistance (R_{ct}), and the slope of the oblique line in low-frequency region reflects the scale of the Warburg impedance (Z_w).[47] The EIS curves of the activated and unactivated samples are fitted using two different models, and the results (**Figure S14,**

Table S1) clearly show that the main barriers during electrochemical reactions are due the value

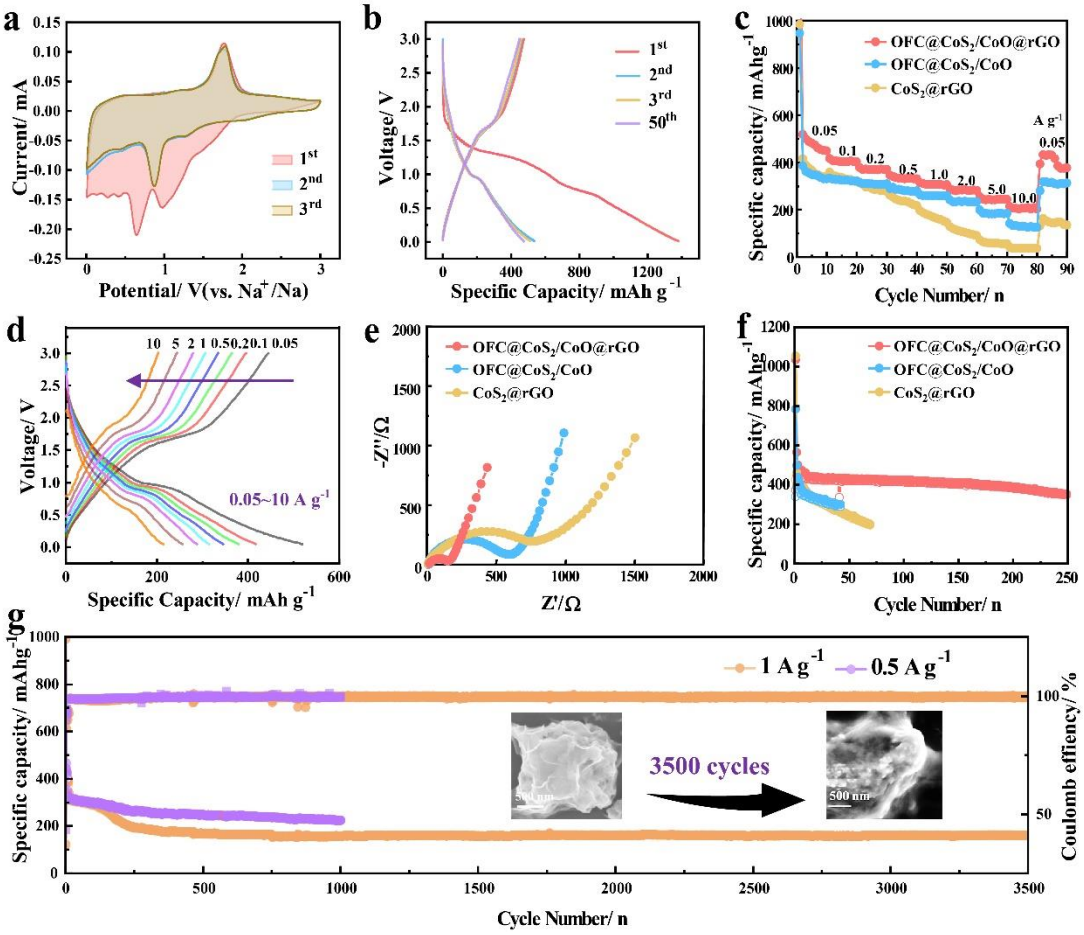

Figure 4. Electrochemical properties. (a) CV curves for the first three cycles at 0.1 mV s^{-1} and (b) voltage profiles for the first three cycles and the 50th cycle at 0.05 A g^{-1} of OFC@CoS_2/CoO@rGO; (c and d) rate performance and its charge/discharge cureves, (e) Nyquist plots, and (f) cycling performance at 0.1 A g^{-1} of the control and target samples; (g) long-term cycling performance of OFC@CoS_2/CoO@rGO at 0.5 and 1 A g^{-1} for 1000 and 3500 cycles, respectively (inset, SEM images of electrode materials before and after cycling). of R_{ct}. Among all the samples, OFC@CoS_2/CoO@rGO has the smallest values of R_{ct} and Z_w **(Figure 4e)**, indicating its excellent electron transfer

and diffusion capability of Na^+ ions.[48] When the OFC or rGO is absent, the R_{ct} values of the other two materials are increased significantly, demonstrating that the transfer of electrons inside the materials becomes difficult. This may be the main reason for the poor discharge performance of the electrodes of OFC@ CoS_2/CoO and CoS_2@rGO. Results strongly confirm the important role of the dual carbon strategy for the improved electrochemcial performance. In **Figure 4f**, OFC@CoS_2/CoO@rGO still delivers a reversible discharge capacity of 353 mAh g^{-1} over 250 cycles at 0.1 A g^{-1} with a coulomb efficiency of 98.3%. However, an obvious decline of capacity can be observed from the initial several cycles when either OFC or rGO is absent. Therefore, the synergistic effects generated from the dual carbon sources, together with contributions from a stable OFC and conductive rGO are the key reasons for the stable cycling performance of active CoS_2/CoO. Therefore, the capacity of the OFC@CoS_2/CoO@rGO at a smaller current of 0.05 A g^{-1} only shows a slight drop after 100 cycles (**Figure S15**). Long-term cycling property is an important parameter to evaluate the performance of the electrode materials. Charge and discharge cycling tests were performed on OFC@CoS_2/CoO@rGO under a high current density of 0.5 and 1 A g^{-1} and the results are shown in **Figure 4g**. Even after 1000 cycles, a stable capacity of 229 mA g^{-1} is still maintained at a current density of 0.5 A g^{-1} and the Coulomb efficiency is ~99.5% (**Figure S16**). Remarkably, the electrode can still maintain a stable capacity of 161 mAh g^{-1} after a long cycling for 3500 times at a high current density of 1 A g^{-1}; meanwhile, the structures remain stable without apparent damage (**Inset of Figure 4g**). By contrast, both the electrodes of OFC@CoS_2/CoO and CoS_2@rGO show

poor performance with obvious declines during their cycling tests. The specific capacity of OFC@CoS_2/CoO is quickly attenuated to ~60 mAh g^{-1} at 0.05, 0.1, and 1 A g^{-1} (**Figure S17**), and CoS_2@rGO also shows poor stability (**Figure S18**). All the above results demonstrate the superior performance of the OFC@CoS_2/CoO@rGO, which is attributed to the efficiently internal support and electron transport provided by the OFC and the formation of stable interfaces due to the encapsulated rGO.

To reveal the underlying mechanisms of this significantly improved performance, the reaction kinetics were studied using the Dunn method [49, 50]. For the CV curves, the relationship between current (*I*) and scan rate (*v*) can be described using **Equation (4)**, and it can be further changed to **Equation (5)** for the convenience of calculation [51].

$$I = av^b \tag{4}$$

$$log(i) = blog(v) + log(a) \tag{5}$$

where *a* and *b* are the fitting values. When the *b* value is close to 0.5, it indicates that the electrochemical process is controlled by the diffusion process. Whereas when the *b* value is close to 1, the electrochemical reaction process is dominated by capacitive behavior [52]. The CV curves were obtained at different scan rates from 0.1 to 2 mV s^{-1}, and the relationship plots of the *log (i)* and *log (v)* were obtained using the main oxidation peak A and reduction peak B during the discharge/charge processes (**Figure 5a, b**). The calculated *b* values for the OFC@CoS_2/CoO@rGO are 0.7962 and 0.8581 for the reduction and oxidation processes, respectively, which indicates the obvious capacitance behavior during the discharge/charge processes[53, 54]. The contribution ratios of capacitive behavior are further calculated using **Equations (6) and (7)** [55],

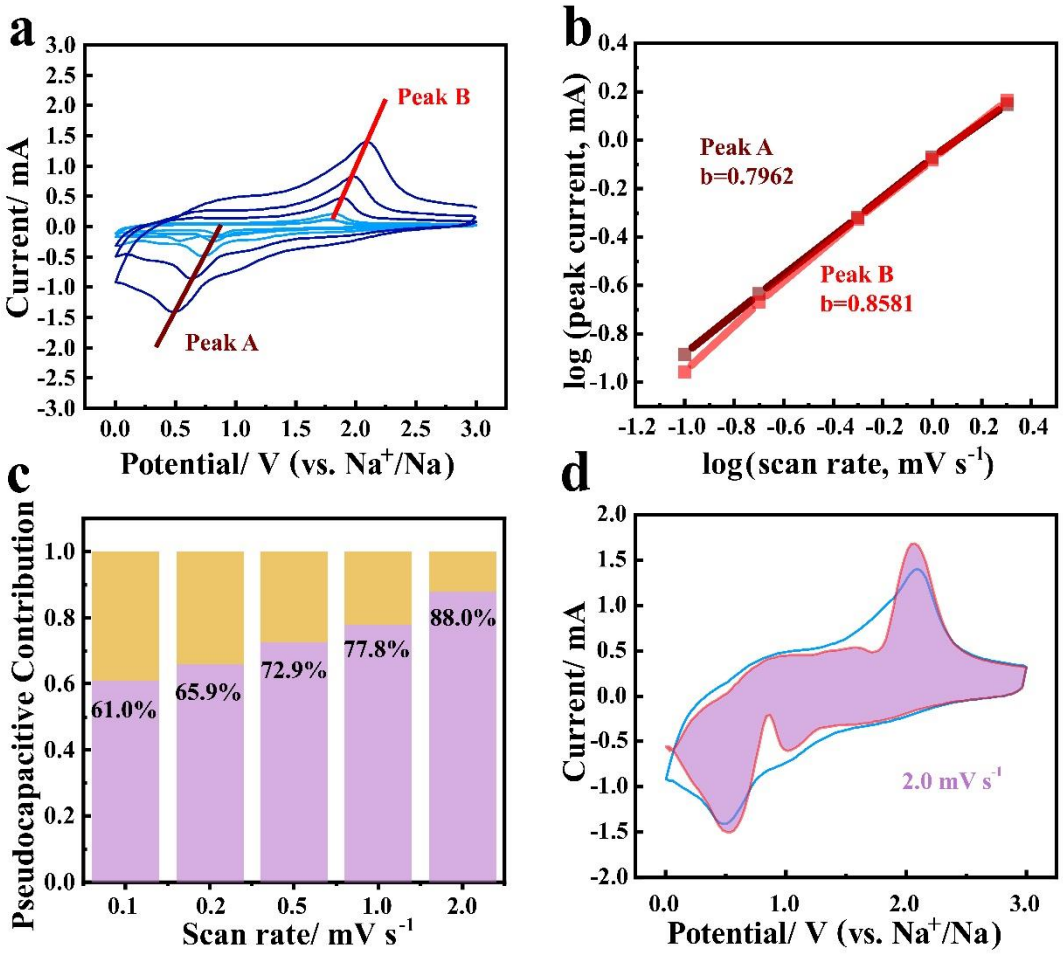

Figure 5. Analysis of electrochemical principle of OFC@CoS_2/CoO@rGO. (a) CV curves at different scan rates; (b) relationship between log(i) and log(v); (c) capacitive and diffusion-controlled contribution ratios at different scan rates; (d) separation of capacitive and diffusion-controlled contribution areas at 2.0 mV s^{-1}.

$$i(V) = k_1 v + k_2 v^{1/2} \quad (6)$$

$$i(V)/v^{1/2} = k_1 v^{1/2} + k_2 \quad (7)$$

where k_1v and $k_2v^{1/2}$ represent the contributions of capacitive and diffusion-controlled behaviors, respectively. The obtained contribution ratios of capacitive behavior (i.e., $k_1v/(k_1v+ k_2v^{1/2})$ are 61.0%, 65.9%, 72.9%, 77.8% and 88%, respectively, at the scan rates of 0.1-2 mV s^{-1} for the OFC@CoS_2/CoO@rGO as shown in **Figure 5c**. The

corresponding contributions of diffusion and capacitive behaviors at various scan rates are visually presented in blue and pink colors in **Figures 5d and S19**. The large *b* values and significant capacitive contributions of OFC@CoS_2/CoO@rGO reveal that the capacitive controlled behavior dominates the whole capacity, especially at high scan rates. This indicates that most redox reactions of Na^+ ions occur on the electrode surface, which enhances the OFC@CoS_2/CoO@rGO to achieve faster charge storage also a better rate performance.

Based on the above analysis, we can summarize that the newly designed OFC@CoS_2/CoO@rGO composites have the following advantages to enhance the anode performances of SIBs:

(1) The rigid OFC with run-through macro-pores offers good conductivity and enhances the storage of Na^+ ions, which are favorable for the pervasion of electrolyte and the delivery of electrons[37];

(2) The mesoporous CoS_2/CoO not only has a good Na^+ storage capacity, but also effectively restricts the volume expansion and reduces the stress during the cycling processes, both of which are beneficial to enhancing the anode performance of the SIBs[56, 57];

(3) The rGOs are encapsulated strongly surrounding the OFC@CoS_2/CoO composite. They stabilize the active CoS_2/CoO, and reduce the formation of excessive solid electrolyte interphase **(SEI)** film and loss of capacity decay. They also provide an excellent electron delivery route and promote the uniform distribution of electrons on

the surface of the material. All of these facilitate the significantly enhanced rate performance[58].

4. Conclusion

In conclusion, the sandwich structure of OFC@CoS_2/CoO@rGO is successfully fabricated by integrating dual carbon skeletons and highly active heterojunctions of CoS_2/CoO, which significantly improves both specific capacity and cycling stability as the anode material for the SIB. Such structures have merits of high reaction activity, accelerated kinetics, and structure stability. As a result, it can deliver a high capacity of 353 mAh g^{-1} at a 0.10 A g^{-1} after 250 cycles. Remarkably, even after 3,500 times cycling at a high current density of 1.0 A g^{-1}, it can still maintain a reversible capacity of 161 mAh g^{-1}. Such a design strategy can be effectively applied to the designs of other high-performance electrode materials for different types of rechargeable batteries.

ASSOCIATED CONTENT

Supporting Information.

Additional details of Supporting Information are presented: Table S1 and figures (Figure S1-S19).

AUTHOR INFORMATION

Corresponding Author

E-mail address: m_wen@tongji.edu.cn (Ming Wen*).

Author Contributions

‡These authors contributed equally to this work.

Ran Sui: Writing-original draft preparation, Investigation, Performances tests, Software, Methodology. The lead of contribution.

Guangtao Zan: Formal analysis, Writing-review & editing, Visualization, Methodology. The lead of contribution.

Ming Wen: Conceptualization, Writing-review & editing, Funding acquisition, Project administration, Supervision. The lead of contribution.

Weina Li: Investigation, Visualization. The supporting of contribution.

Zihui Liu: Visualization. The supporting of contribution.

Qingsheng Wu: Conceptualization, Methodology. The supporting of contribution.

YongQing Fu: Writing-review & editing, Funding acquisition. The supporting of contribution.

ACKNOWLEDGMENT

This work was financially supported by the National Natural Science Foundation (NSFC Nos: 22171212), Science and Technology Committee of Shanghai Municipality (21160710300, 19DZ2271500) by China, International Exchange Grant (IEC/NSFC/201078) through Royal Society UK and NSFC.

REFERENCES

(1) Dunn, B.; Kamath, H.; Tarascon, J.-M. Electrical Energy Storage for the Grid: A Battery of Choices. *Science* **2011**, *334* (6058), 928-935.

(2) Wang, S.; Sun, C.; Wang, N.; Zhang, Q. Ni- and/or Mn-Based Layered Transition Metal Oxides as Cathode Materials for Sodium Ion Batteries: Status, Challenges and Countermeasures. *J. Mater. Chem. A* **2019**, *7* (17), 10138-10158.

(3) Xu, J.; Dou, S.; Wang, Y.; Yuan, Q.; Deng, Y.; Chen, Y. Development of Metal and Metal-Based Composites Anode Materials for Potassium-Ion Batteries. *Transactions of Tianjin University* **2021**, *27* (3), 248-268.

(4) Fang, Y.; Xiao, L.; Chen, Z.; Ai, X.; Cao, Y.; Yang, H. Recent Advances in Sodium-Ion Battery Materials. *Electrochemical Energy Reviews* **2018**, *1* (3), 294-323.

(5) Fan, L.; Li, X.; Yan, B.; Feng, J.; Xiong, D.; Li, D.; Gu, L.; Wen, Y.; Lawes, S.; Sun, X. Controlled SnO_2 Crystallinity Effectively Dominating Sodium Storage Performance. *Adv. Energy Mater.* **2016**, *6* (10), 1502057.

(6) Zhang, Y.; Wang, N.; Sun, C.; Lu, Z.; Xue, P.; Tang, B.; Bai, Z.; Dou, S. 3D Spongy CoS_2 Nanoparticles/Carbon Composite as High-performance Anode Material for Lithium/Sodium Ion Batteries. *Chem. Eng. J.* **2018**, *332*, 370-376.

(7) Xiao, B.; Rojo, T.; Li, X. Hard Carbon as Sodium-Ion Battery Anodes: Progress and Challenges. *ChemSusChem* **2019**, *12* (1), 133-144.

(8) Yabuuchi, N.; Kubota, K.; Dahbi, M.; Komaba, S. Research Development on Sodium-Ion Batteries. *Chem. Rev.* **2014**, *114* (23), 11636-11682.

(9) Lao, M.; Zhang, Y.; Luo, W.; Yan, Q.; Sun, W.; Dou, S. X. Alloy-Based Anode Materials toward Advanced Sodium-Ion Batteries. *Adv. Mater.* **2017**, *29* (48), 1700622.

(10) Balogun, M.-S.; Luo, Y.; Qiu, W.; Liu, P.; Tong, Y. A Review of Carbon Materials and their Composites with Alloy Metals for Sodium Ion Battery Anodes. *Carbon* **2016**, *98*, 162-178.

(11) Xiao, L.; Lu, H.; Fang, Y.; Sushko, M. L.; Cao, Y.; Ai, X.; Yang, H.; Liu, J. Low-Defect and Low-Porosity Hard Carbon with High Coulombic Efficiency and High Capacity for Practical Sodium Ion Battery Anode. *Adv. Energy Mater.* **2018**, *8* (20), 1703238.

(12) Hirsh, H. S.; Sayahpour, B.; Shen, A.; Li, W.; Lu, B.; Zhao, E.; Zhang, M.; Meng, Y. S. Role of Electrolyte in Stabilizing Hard Carbon as an Anode for Rechargeable Sodium-Ion Batteries with Long Cycle Life. *Energy Stor. Mater.* **2021**, *42*, 78-87.

(13) Pan, Q.; Tong, Z.; Su, Y.; Qin, S.; Tang, Y. Energy Storage Mechanism, Challenge and Design Strategies of Metal Sulfides for Rechargeable Sodium/Potassium-Ion Batteries. *Adv. Funct. Mater.* **2021**, *31* (37), 2103912.

(14) Dou, S.; Xu, J.; Cui, X.; Liu, W.; Zhang, Z.; Deng, Y.; Hu, W.; Chen, Y. High‐Temperature Shock Enabled Nanomanufacturing for Energy-Related Applications. *Adv. Energy Mater.* **2020**, *10* (33), 2001331.

(15) Chen, S.; Xing, K.; Wen, J.; Wen, M.; Wu, Q.; Cui, Y. Hierarchical Assembly and Superior Sodium Storage Properties of a Sea-Sponge Structured C/SnS@C Nanocomposite. *J. Mater. Chem. A* **2018**, *6* (17), 7631-7638.

(16) Dou, S.; Xu, J.; Sari, H. M. K.; Wu, H.-H.; Hu, J.; Zhang, Y.; Fan, L.; Xiong, D.; Zhou, W.; Chen, Y.; Li, X. Large Interlayer Spacing of Few-Layered Cobalt–Tin-Based Sulfide Providing Superior Sodium Storage. *ACS Appl. Mater. Inter.* **2020**, *12* (37), 41546-41556.

(17) Cao, L.; Gao, X.; Zhang, B.; Ou, X.; Zhang, J.; Luo, W.-B. Bimetallic Sulfide Sb_2S_3@ FeS_2 Hollow Nanorods as High-Performance Anode Materials for Sodium-Ion Batteries. *ACS Nano* **2020**, *14* (3), 3610-3620.

(18) Xiao, Y.; Lee, S. H.; Sun, Y. K. The Application of Metal Sulfides in Sodium Ion Batteries. *Adv. Energy Mater.* **2017**, *7* (3), 1601329.

(19) David, L.; Bhandavat, R.; Singh, G. MoS_2/Graphene Composite Paper for Sodium-Ion Battery Electrodes. *ACS Nano* **2014**, *8* (2), 1759-1770.

(20) Li, Y.; Sun, X.; Cheng, Z.; Xu, X.; Pan, J.; Yang, X.; Tian, F.; Li, Y.; Yang, J.; Qian, Y. Mesoporous $Cu_{2-x}Se$ Nanocrystals as an Ultrahigh-Rate and Long-Lifespan Anode Material for Sodium-Ion Batteries. *Energy Stor. Mater.* **2019**, *22*, 275-283.

(21) Shadike, Z.; Cao, M.-H.; Ding, F.; Sang, L.; Fu, Z.-W. Improved Electrochemical Performance of CoS_2–MWCNT Nanocomposites for Sodium-Ion Batteries. *Chem. Commun.* **2015**, *51* (52), 10486-10489.

(22) Rahman, M. M.; Glushenkov, A. M.; Ramireddy, T.; Chen, Y. Electrochemical Investigation of Sodium Reactivity with Nanostructured Co_3O_4 for Sodium-Ion Batteries. *Chem. Commun.* **2014**, *50* (39), 5057-5060.

(23) Long, Y.; Yang, J.; Gao, X.; Xu, X.; Fan, W.; Yang, J.; Hou, S.; Qian, Y. Solid-Solution Anion-Enhanced Electrochemical Performances of Metal Sulfides/Selenides for Sodium-Ion Capacitors: The Case of $FeS_{2-x}Se_x$. *ACS Appl. Mater. Inter.* **2018**, *10* (13), 10945-10954.

(24) Zhang, T.; Ran, F. Design Strategies of 3D Carbon-Based Electrodes for Charge/Ion Transport in Lithium Ion Battery and Sodium Ion Battery. *Adv. Funct. Mater.* **2021**, *31* (17), 2010041.

(25) Sun, R.; Wei, Q.; Li, Q.; Luo, W.; An, Q.; Sheng, J.; Wang, D.; Chen, W.; Mai, L. Vanadium Sulfide on Reduced Graphene Oxide Layer as a Promising Anode for Sodium Ion Battery. *ACS Appl. Mater. Inter.* **2015**, *7* (37), 20902-20908.

(26) Feng, Y.; Xu, M.; He, T.; Chen, B.; Gu, F.; Zu, L.; Meng, R.; Yang, J. CoPSe: A New Ternary Anode Material for Stable and High-Rate Sodium/Potassium-Ion Batteries. *Adv. Mater.* **2021**, *33* (16), 2007262.

(27) Jache, B.; Binder, J. O.; Abe, T.; Adelhelm, P. A Comparative Study on the Impact of Different Glymes and their Derivatives as Electrolyte Solvents for Graphite Co-intercalation Electrodes in Lithium-Ion and Sodium-Ion Batteries. *Phys. Chem. Chem. Phys.* **2016**, *18* (21), 14299-14316.

(28) Dong, Y.; Shi, W.; Lu, P.; Qin, J.; Zheng, S.; Zhang, B.; Bao, X.; Wu, Z.-S. 2D Holey Cobalt Sulfide Nanosheets Derived from Metal–Organic Frameworks for High-Rate Sodium Ion Batteries with Superior Cyclability. *J. Mater. Chem. A* **2018**, *6* (29), 14324-14329.

(29) Hu, C.; Zhu, Y.; Ma, G.; Tian, F.; Zhou, Y.; Yang, J.; Qian, Y. Sandwich-Structured Dual Carbon Modified Bismuth Nanosphere Composites as Long-Cycle and High-Rate Anode Materials for Sodium-Ion Batteries. *Electrochim. Acta* **2021**, *365*, 137379.

(30) Wang, J.; Liu, D.-H.; Wang, Y.-Y.; Hou, B.-H.; Zhang, J.-P.; Wang, R.-S.; Wu, X.-L. Dual-Carbon Enhanced Silicon-Based Composite as Superior Anode Material for Lithium Ion Batteries. *J. Power Sources* **2016**, *307*, 738-745.

(31) Yuan, S.; Huang, X. l.; Ma, D. l.; Wang, H. g.; Meng, F. z.; Zhang, X. b. Engraving Copper Foil to Give Large-Scale Binder-Free Porous CuO Arrays for a High-Performance Sodium-ion Battery Anode. *Adv. Mater.* **2014**, *26* (14), 2273-2279.

(32) Liu, X.; Zhang, K.; Lei, K.; Li, F.; Tao, Z.; Chen, J. Facile Synthesis and Electrochemical Sodium Storage of CoS_2 Micro/Nano-Structures. *Nano Res.* **2016**, *9* (1), 198-206.

(33) Yu, L.; Yang, J. F.; Lou, X. W. Formation of CoS_2 Nanobubble Hollow Prisms for Highly Reversible Lithium Storage. *Angew. Chem. Int. Ed.* **2016**, *55* (43), 13422-13426.

(34) Kaneti, Y. V.; Zhang, J.; He, Y.-B.; Wang, Z.; Tanaka, S.; Hossain, M. S. A.; Pan, Z.-Z.; Xiang, B.; Yang, Q.-H.; Yamauchi, Y. Fabrication of an MOF-Derived Heteroatom-Doped Co/CoO/Carbon Hybrid with Superior Sodium Storage Performance for Sodium-Ion Batteries. *J. Mater. Chem. A* **2017**, *5* (29), 15356-15366,

(35) Cai, X.; Lai, L.; Shen, Z.; Lin, J. Graphene and Graphene-Based Composites as Li-Ion battery Electrode Materials and their Application in Full Cells. *J. Mater. Chem. A* **2017**, *5* (30), 15423-15446.

(36) Zan, G.; Wu, T.; Zhu, F.; He, P.; Cheng, Y.; Chai, S.; Wang, Y.; Huang, X.; Zhang, W.; Wan, Y. A Biomimetic Conductive Super-Foldable Material. *Matter* **2021**, *4* (10), 3232-3247.

(37) Li, W.; Li, J.; Wen, J.; Wen, M.; Chen, S.; Wu, Q.; Fu, Y. Hollow Nanostructure of Sea-Sponge-C/SiC@ SiC/C for Stable Li^+-Storage Capability. *Sci. Bull.* **2019**, *64* (16), 1152-1157.

(38) Xiong, W.; Huang, W.; Zhang, M.; Hu, P.; Cui, H.; Zhang, Q. Pillar[5]quinone–Carbon Nanocomposites as High-Capacity Cathodes for Sodium-Ion Batteries. *Chem. Mater.* **2019**, *31* (19), 8069-8075.

(39) Marcano, D. C.; Kosynkin, D. V.; Berlin, J. M.; Sinitskii, A.; Sun, Z.; Slesarev, A.; Alemany, L. B.; Lu, W.; Tour, J. M. Improved Synthesis of Graphene Oxide. *ACS Nano* **2010**, *4* (8), 4806-4814.

(40) Aguilar-Bolados, H.; Vargas-Astudillo, D.; Yazdani-Pedram, M.; Acosta-Villavicencio, G.; Fuentealba, P.; Contreras-Cid, A.; Verdejo, R.; López-Manchado, M. A. Facile and Scalable One-Step Method for Amination of Graphene Using Leuckart Reaction. *Chem. Mater.* **2017**, *29* (16), 6698-6705.

(41) Chai, S.; Zan, G.; Dong, K.; Wu, T.; Wu, Q. Approaching Superfoldable Thickness-Limit Carbon Nanofiber Membranes Transformed from Water-Soluble PVA. *Nano Lett.* **2021**, *21* (20), 8831-8838.

(42) Zan, G.; Wu, T.; Zhang, Z.; Li, J.; Zhou, J.; Zhu, F.; Chen, H.; Wen, M.; Yang, X.; Peng, X. Bioinspired Nanocomposites with Self-Adaptive Stress Dispersion for Super-Foldable Electrodes. *Adv. Sci.* **2022**, *9* (3), 2103714.

(43) Fang, Y.; Luan, D.; Chen, Y.; Gao, S.; Lou, X. W. Synthesis of Copper-Substituted CoS_2@ Cu_xS Double-Shelled Nanoboxes by Sequential Ion Exchange for Efficient Sodium Storage. *Angew. Chem. Int. Ed.* **2020**, *59* (7), 2644-2648.

(44) Yin, J.; Li, Y.; Lv, F.; Lu, M.; Sun, K.; Wang, W.; Wang, L.; Cheng, F.; Li, Y.; Xi, P. Oxygen Vacancies Dominated NiS_2/CoS_2 Interface Porous Nanowires for Portable Zn–Air Batteries Driven Water Splitting Devices. *Adv. Mater.* **2017**, *29* (47), 1704681.

(45) Zhu, Y.; Han, X.; Xu, Y.; Liu, Y.; Zheng, S.; Xu, K.; Hu, L.; Wang, C. Electrospun Sb/C Fibers for a Stable and Fast Sodium-Ion Battery Anode. *ACS Nano* **2013**, *7* (7), 6378-6386.

(46) He, H.; Sun, D.; Tang, Y.; Wang, H.; Shao, M. Understanding and Improving the Initial Coulombic Efficiency of High-Capacity Anode Materials for Practical Sodium Ion Batteries. *Energy Stor. Mater.* **2019**, *23*, 233-251.

(47) Zhang, H.; Guo, H.; Li, A.; Chang, X.; Liu, S.; Liu, D.; Wang, Y.; Zhang, F.; Yuan, H. High Specific Surface Area Porous Graphene Grids Carbon as Anode Materials for Sodium Ion Batteries. *J. Energy Chem.* **2019**, *31*, 159-166.

(48) Gu, S.; Wu, S.; Cao, L.; Li, M.; Qin, N.; Zhu, J.; Wang, Z.; Li, Y.; Li, Z.; Chen, J. Tunable Redox Chemistry and Stability of Radical Intermediates in 2D Covalent Organic Frameworks for High Performance Sodium Ion Batteries. *J. Am. Chem. Soc.* **2019**, *141* (24), 9623-9628.

(49) Wang, J.; Polleux, J.; Lim, J.; Dunn, B. Pseudocapacitive Contributions to Electrochemical Energy Storage in TiO_2 (Anatase) Nanoparticles. *J. Phy. Chem. C* **2007**, *111* (40), 14925-14931.

(50) Choi, C.; Ashby, D. S.; Butts, D. M.; DeBlock, R. H.; Wei, Q.; Lau, J.; Dunn, B. Achieving High Energy Density and High Power Density with Pseudocapacitive Materials. *Nat. Rev. Mater.* **2020**, *5* (1), 5-19.

(51) Hou, T.; Liu, B.; Sun, X.; Fan, A.; Xu, Z.; Cai, S.; Zheng, C.; Yu, G.; Tricoli, A. Covalent Coupling-Stabilized Transition-Metal Sulfide/Carbon Nanotube Composites for Lithium/Sodium-Ion Batteries. *ACS Nano* **2021**, *15* (4), 6735-6746.

(52) Wang, S.; Cao, F.; Li, Y.; Zhang, Z.; Zhou, D.; Yang, Y.; Tang, Z. MoS_2-Coupled Carbon Nanosheets Encapsulated on Sodium Titanate Nanowires as Super-Durable Anode Material for Sodium-ion Batteries. *Adv. Sci.* **2019**, *6* (10), 1900028.

(53) Yang, J.; Gao, H.; Men, S.; Shi, Z.; Lin, Z.; Kang, X.; Chen, S. $CoSe_2$ Nanoparticles Encapsulated by N-doped Carbon Framework Intertwined with Carbon Nanotubes: High-Performance Dual-Role Anode Materials for Both Li- and Na-Ion Batteries. *Adv. Sci.* **2018**, *5* (12), 1800763.

(54) Guangtao Zan, Tong Wu, Wenya Dong, Junchen Zhou, Teng Tu, Ruoxuan Xu, Yun Chen, Ying Wang, Qingsheng Wu. Two-Level Biomimetic Designs Enable Intelligent Stress Dispersion for Super-Foldable C/NiS Nanofiber Free-Standing Electrode. *Adv. Fiber Mater.* **2022**, DOI: 10.1007/s42765-022-00162-7.

(55) Zhang, Y.; Li, J.; Ma, L.; Li, H.; Xu, X.; Liu, X.; Lu, T.; Pan, L. Insights into the Storage Mechanism of 3D Nanoflower-Like V_3S_4 Anode in Sodium-Ion Batteries. *Chem. Eng. J.* **2022**, *427*, 130936.

(56) Lin, X.; Zhang, T.; Chu, C.; Li, Z.; Liu, R.; Li, P.; Li, Y.; Huang, Z.; Ma, Y. Synthesis of ZIF-Derived CoS_2 Nanocages Interconnected by CNTs for Rechargeable Li–O_2 Batteries. *ACS Sustain. Chem. Eng.* **2020**, *8* (20), 7581-7587.

(57) Ma, Y.; Ma, Y.; Bresser, D.; Ji, Y.; Geiger, D.; Kaiser, U.; Streb, C.; Varzi, A.; Passerini, S. Cobalt Disulfide Nanoparticles Embedded in Porous Carbonaceous Micro-polyhedrons Interlinked by Carbon Nanotubes for Superior Lithium and Sodium Storage. *ACS Nano* **2018**, *12* (7), 7220-7231.

(58) Men, S.; Zheng, H.; Ma, D.; Huang, X.; Kang, X. Unraveling the Stabilization Mechanism of Solid Electrolyte Interface on ZnSe by rGO in Sodium Ion Battery. *J. Energy Chem.* **2021**, *54*, 124-130.

Table of Contents